

Model for hot spots induced by surface electric fields in superconducting rf cavities

Aymeric Ramiere¹ and Jay Amrit^{2*}

¹School of Physics and Optoelectronic Engineering, Shenzhen University, Shenzhen, 518060, China

²Laboratoire d'Informatique pour la Mécanique et les Sciences de l'Ingénieur, LIMSI-CNRS, Université Paris-Saclay, Rue John von Neumann, 91403, Orsay, France

*E-mail : jay.amrit@limsi.fr

Abstract

Hot spots in niobium superconducting radio-frequency (SRF) cavities are important sources of heat dissipation. Tracking their physical origin is the key to controlling and improving SRF cavity performance. In this paper, we present a new model to explain the occurrence of hot spots in niobium SRF cavities based on an electro-thermal mechanism which is analogous to the phenomenon leading to the coherer effect. In our model, the localized punctual heat dissipation is induced by the presence of the residual electric field in the inner surface of the cavity wall. We derive an equation for the temperature of hot spots as a function of the local surface electric field \vec{E}_y and key parameters which include the London penetration depth $\lambda_L(T)$, the frequency f of the accelerating field E_a and the size ϕ of a hot spot. Our model gives new insight about the occurrence of hot spots and clarifies the role of grains boundaries and micro-cracks in the inner surface of the cavity wall. It also provides a convincing explanation of the experimental data on Q-drop and reveals for the first time the importance of the electric component \vec{E}_y associated to the rf magnetic field \vec{B}_z parallel to the inner Nb surface. A spin-off result of our model reveals an origin of the BCS surface resistance dependence on the surface magnetic field.

Keywords: hot spots, SRF cavity, electric field, grain boundary, Q-drop

1. Introduction

The occurrence of local punctual overheating, called hot spots, in superconducting radio-frequency (SRF) cavities made of niobium, is an important dissipative phenomenon which propagates in the walls and lead to a sharp drop in the quality factor Q (also called Q-drop) at high accelerating fields (> 25 MV/m) [1,2]. The quality factor of a cavity is defined as $Q = \omega U/P$, where U is the stored energy and (P/ω) the total power loss in the inner walls in one rf radian. The quality factor is also expressed as $Q = G/R_s$, where G a geometrical factor described only by the cavity shape and R_s is the residual surface resistance determined by the BCS surface resistance. The global power loss scheme in SRF cavities is due to Joule dissipation on the inner walls of the cavity when the magnetic field interacts with electrons. This power loss is defined by $P_j = \frac{1}{2\mu_0^2} R_s B^2$, where μ_0 is the magnetic permeability of free space and B is the magnetic field.

For over two decades, a substantial amount of effort has been invested to understand and control heat dissipation in the walls of SRF niobium cavities when subjected to electromagnetic fields. Ciovatti and Gurevich [3] described the origin of the high field Q-drop and conjectured that it is related to the field dependent behavior of the BCS term in the surface resistance. When the rf magnetic field amplitude H_{RF} approaches the superconductor critical field H_C , both the normal electron density and the BCS surface resistance R_{BCS} increase due to the effect of current pair-breaking on thermal activation, which in turn increases heating, thus making R_{BCS} non-linear in high fields. For type II superconductors like Nb, in the clean limit (i.e. when the phonon mean free path is greater than the BCS coherence length) and at low frequency, the high-field nonlinear correction increases exponentially with field and temperature, and thereby gives rise to thermal runaway [1,4,5].

In reality, the non-uniform thermal breakdown process described by Gurevich [4] is ignited by hot spots. Tracking the physical origin of hot spots is also the key to designing/adopting appropriate material treatments to improve and thereby control cavity performance from a thermal point of view. Various models have been proposed and in almost all the models the magnetic field [6,7] plays a decisive role. In the magnetic enhancement model, sharp corners and edges at grain boundaries on the superconducting Nb surface transit to normal-conducting state because of the local magnetic field. In later studies, the generation of hot spots due to magnetic vortices oscillating in the presence of high rf fields has been extensively examined [8]. This

latter model, in particular, explains the presence of hot spots observed on cavities where bundles of trapped vortices can produce localized dissipative regions from where heat spreads over several tens of mm. The magnetic vortices are either remnants of the Earth's magnetic field or are induced by thermoelectric currents during cooling of Nb below T_c . These vortices are trapped on the Nb surface at grain boundaries, defects, impurities... The possibility of depinning these vortices by subjecting them to a thermal "force" gradient has been experimentally demonstrated [3]. Finally, we note that to our knowledge the only other models which attribute the origin of hot spots to the presence of an electric field, is the interface tunnel exchange model, developed by independently by Halbritter [9,10] and by T. Junginger *et al.* [11, 12]. We shall refer to this later. A more recent study shows the importance of the electric field on rf losses due to the presence of niobium pentoxide [13].

A review of the present status in the high field Q-slope and quench field problem is given in chapter 5 of ref. [14] and in refs. [15, 16] and references herein. Among all the different models which have been proposed, none of them give a comprehensive and predictive description of the mechanism of hot spot formation. It is now generally admitted that more than one mechanism leads to the formation of hot spots. And, it is also highly likely that these mechanisms are active simultaneously. Consequently, there is a necessity to clearly identify the different mechanisms and to evaluate their interconnectedness to control Q-losses in SRF cavities.

In this paper, we formulate a new dissipative mechanism due to the penetration of the surface electric field into the inner surface of the SRF cavity wall. Our model is derived from the coherer effect which relates to an important change of the electrical resistance of a granular medium when an electromagnetic wave is produced in its vicinity. Experimental studies [17,18] provide a comprehensive understanding of the transition in the electrical conduction (and resistance) in granular medium. One important origin of the electrical resistance has been identified to be oxide layers and/or impurities at the contact areas between grains. In this case, local Joule heating due to the presence of an electric field leads to sufficiently high temperatures which destroy the oxide layers and induces welding of contacts, thereby reducing the electrical resistance to current flow and increasing the surface area [19].

This paper is organized as follows. Firstly, we describe our model configuration for localized ohmic heating at a contact site. The temperature increase at a hot spot is then derived as a function of the local

surface electric field E_y associated to the surface magnetic field B_z of frequency f , the hot spot size ϕ and the temperature dependent London penetration depth $\lambda_L(T)$. Numerical applications are carried out using polycrystalline niobium as the material for the cavity wall. The various tendencies predicted by our model are then discussed : the size of hot spots which come into play at different hot spot temperatures T_h , the behavior of $T_h(\phi)$ as a function of surface magnetic field B_z , the evolution of the maximum critical surface magnetic fields B_Q for different ϕ and bath temperatures; and estimations of power dissipation and current densities as a function of B_z for different ϕ . A quantitative comparison is made to experimental data found in the literature to demonstrate the plausibility of our new mechanism.

2. Model for hot spot generation by surface electric field

The present scenario is based on the fact that portions of grain boundaries in polycrystalline or cracks in single crystal niobium may constitute possible contact sites/loci for heat dissipation when subjected to electric fields (see Fig. 1 (a)). Under critical conditions, which we shall establish, hot spots form at these contact sites. To derive the equation of the temperature of a hot spot, we consider that local Joule heating is taking place at these sites. The electrical resistance at these contact sites is also an important parameter.

Let the y - z plane lie on the inner surface of a polycrystalline niobium wall of a cavity. For simplicity, we shall consider two grains in contact as shown schematically in Fig. 1 (b). In the presence of an *in-plane* surface electric field \vec{E}_y , the electron current lines taper as they pass through the contact site between two grains. The local electrical power dissipation due to the Joule effect is $P_E = RI^2 = U^2/R$, where I is the electrical current flowing across the contact site, R is the electrical resistance associated to the contact site and U is the local electrical potential (voltage drop) which is established across the contact as shown in Fig. 1 (b). The bulk electrical resistance inside each grain is negligible. Under steady state conditions, the heat produced P_E leads to a local temperature maximum T_h at the contact site that we now refer to as the hot spot. The temperature far away from the hot spot in each grain is T_0 . The electrical heat dissipated at the hot spot is equally shared by thermal conduction between the two grains and is carried from T_h to T_0 in each grain. The electrical and thermal currents have the coinciding paths. In a straightforward 1D derivation, the energy balance is written as:

$$-\kappa A \frac{dT}{dx} = \frac{U^2}{R} \quad (1)$$

where T is the temperature, κ is the thermal conductivity and A is the cross-sectional contact area. The change in the electrical resistance $dR = \rho \frac{dx}{A} = \frac{dU}{I}$, where ρ is the electrical resistivity. Eq. (1) can now be written as:

$$-\kappa \rho dT = U dU \quad (2)$$

Since the electrical resistivity and the thermal conductivity are due to electron flow, we can use the Wiedemann-Franz law $\kappa \rho = LT$, where L is the Lorentz constant. Integrating Eq. (2) from T_h to T_0 , we get:

$$T_h^2 = T_0^2 + \frac{\varphi^2}{4L} \quad (3)$$

where $U(T_0) = \pm \frac{\varphi}{2}$ is the potential drop between T_h and T_0 in each grain. Equation (3) is in fact the Kohlrusch equation [18] which characterizes the temperature-voltage drop relationship for metallic contacts. The Lorentz constant in most metals is generally equal to the theoretical value $L_0 = 2.45 \times 10^{-8} \text{ (V}^2/\text{K}^2\text{)}$. For Nb in the superconducting state, it is shown that the Lorentz constant $L = 2.05 \times 10^{-8} \text{ (V}^2/\text{K}^2\text{)}$ for $1.8 < T < 9.2 \text{ K}$ [20]. Considering the smallness of the Lorentz constant value, a small increase in the potential drop across the contact will lead to a substantial increase in temperature of the hot spot.

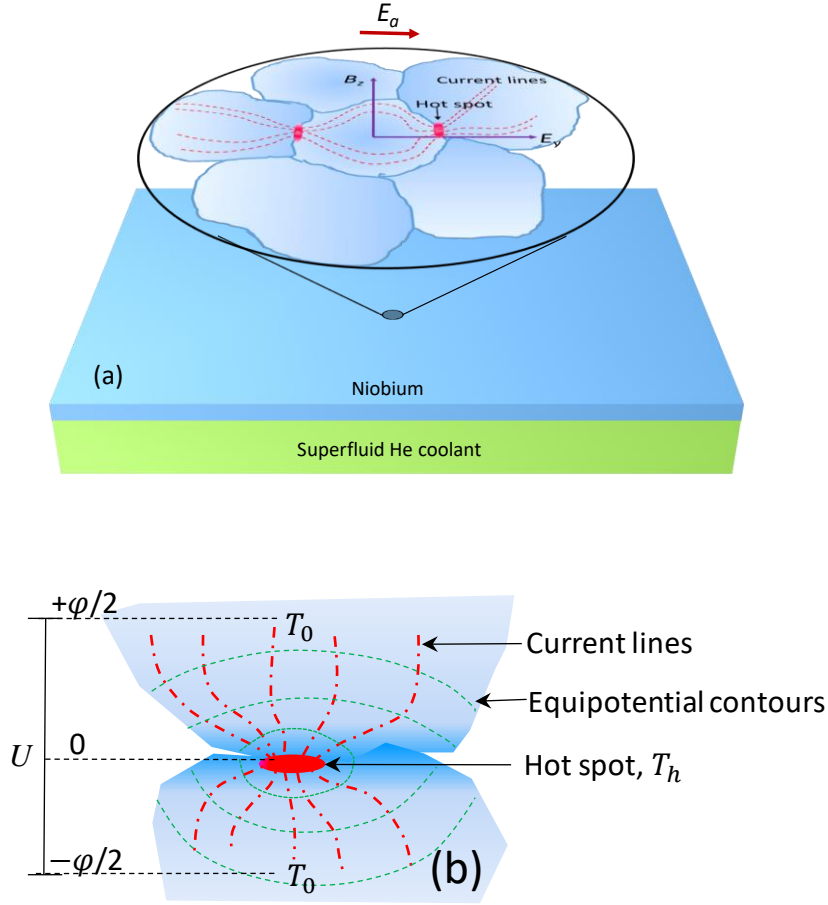


Figure 1. (a). Sketch showing a zoom of two hot spots at some portions of grain boundaries in polycrystalline niobium cooled by superfluid He. Dashed lines depict current lines in the element of cavity wall (b) Schematics showing formation of a hot spot at a contact site between two grain boundaries in polycrystalline Nb. The voltage drop $U(T)$ between T_h and T_0 in each grain is equal to $\phi/2$. (color online)

The magnitude of the local potential drop ϕ is given by the line integral of the surface electric field E_y as seen by the electrons that are “squeezed” to pass through the contact site, that is, $\phi = \int_0^\phi E_y dy = E_y \phi$, where ϕ corresponds in length to the diameter of the contact between the two grains. As shown in Fig. 1 (b), ϕ corresponds to a fraction of the grain size. From Eq. (3), the temperature of the hot spot is now given by:

$$T_h = \left(T_0^2 + \frac{E_y^2 \phi^2}{4L} \right)^{\frac{1}{2}} \quad (4)$$

The relationship between the surface electric field E_y and the temperature of the hot spot becomes clearly highlighted. An important feature also emerging from Eq. (4) is the T_h dependency on the size of the contact ϕ .

Now, the tangential electric field E_y is induced by the rf magnetic field B_z in the plane of the surface. According to the Maxwell equation $\nabla \times \vec{E} = -\frac{\partial \vec{B}}{\partial t}$, we have $E_y = -j\omega\lambda_L B_z$, where $\omega = 2\pi f$ is the angular frequency. Replacing in Eq. (4) now yields:

$$T_h^2 = T_0^2 + \frac{(2\pi f)^2 \lambda_L^2(T_h) B_z^2 \phi^2}{4L} \quad (5)$$

In this form the above equation characterizes the formation of hot spots in terms of well-known parameters of the SRF cavity and the contact size ϕ between grains. We have also explicitly indicated the temperature dependency of the London penetration depth $\lambda_L(T_h) = \lambda_0/[1 - (T_h/T_c)^4]^{1/2}$ with $\lambda_0 \approx 30$ nm. As we shall see later, $\lambda_L(T)$ plays a critical role in thermal runaway, especially as T_h approaches the Nb transition temperature T_c . In our model, the size of the hot spot is determined by the magnitude of electric field E_y across the contact and the nature (electrical resistance and geometrical form) of the contact site between grains. We note that since there can be a distribution of contact sizes in polycrystalline materials, it is therefore possible to have a distribution of hot spot sites, with each at a different temperature.

For elliptical SFR cavities the accelerating gradient $E_a = \frac{B_z}{4}$ (mT) and therefore equation (5) becomes :

$$T_h^2 = T_0^2 + \frac{(4\pi f)^2 \lambda_0^2 E_a^2 \phi^2}{L[1 - (T_h/T_c)^4]} \quad (6)$$

Eq. (6) gives a global description of the phenomenon by linking the increase in the hot spot temperature to the accelerating gradient E_a .

Finally, we note that for the Wiedemann-Franz law to hold, the mean free paths for both the electrical and the thermal conductivities must be identical. The electrical resistivity of niobium can be expressed as $\rho = \rho_0 + \rho_{ph}(T) + \rho_{mag}$ where the temperature independent ρ_0 is the residual resistivity due to impurities,

grain boundaries and dislocations and ρ_{mag} is the resistivity in a magnetic field. The phonon contribution at $T < 25$ K can be approximated as $\rho_{ph}(T) = 6.5 \times 10^{-6} T^3 \mu\Omega \text{ cm}$ [21]. When Nb is in the superconducting state at $T < T_c \approx 9.2$ K, we have $\rho \approx \rho_0$ and the mean free paths for electrical and thermal conductivities can be clearly assumed to be the same and hence the Wiedemann-Franz law is applicable.

3. Results

3.1. Conditions for localized heating due to voltage drop

The presence of a voltage drop is the predominant requirement for heating to occur at contacts owing to the onset of the coherer effect. We determine the magnitude of the voltage drops as a function of the contact temperature T_h using equation 3. In Fig. 2, these voltages are calculated at three different bulk temperatures of the inner wall of the cavity, namely 2 K, 3 K and 4 K.

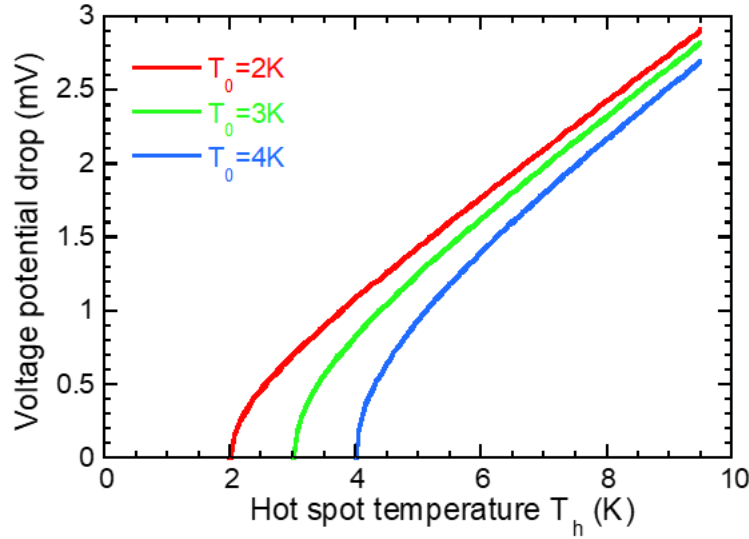


Figure 2. Voltage drop across contacts as function of the hot spot temperature T_h as predicted by Eq. 3. T_0 is the global temperature of the inner surface of the SRF cavity. Voltage drops of the order of 3 mV dissipate sufficient heat so that contacts reach the transition temperature of Nb. The sensitivity of the of the temperature change to voltage drops is clearly revealed. (color online)

Clearly, the influence of the bulk temperatures on the voltage drops remains modest. The salient feature in Fig. 2 is that the formation of hot spots requires local voltages which lie within the range of a fraction of a millivolt to less than ~ 3 mV. For a voltage drop of the order of 0.5 mV, a hot spot can reach a temperature which exceeds the bulk temperature by ~ 500 mK at a working temperature of $T_0 = 2$ K of SRF cavities. When voltage drops of the order of ~ 3 mV are present, the hot spot temperature surpasses the transition temperature of Nb. The sensitivity of the hot spot temperature to the voltage change is ~ 2 K/mV. These small values of the voltage drop suggest that this heating effect can be easily triggered when there exists an electrical resistance at contact spots.

We remark that equation (3) appears void of material properties. This is a consequence of the electron scattering times that contribute to both the electrical and the thermal conductivities [18]. In reality, the local voltage drop is governed by the electrical resistance R at the contact whose magnitude depends entirely on the nature and the geometry of the contact at interfaces. For polycrystalline niobium, R is determined by the properties and the contact area geometry in the presence of impurities (O, H, NbO...) at grain boundaries. In the case of single crystals, the surface roughness and/or crack depths shall also determine the contact area geometry. In the absence of impurities or an oxide layer, the contact between grains may form a link constriction junction (also called a “point” contact) where once again the geometry impacts the value of R .

3.2. Sizes and temperatures of hot spots

The sizes ϕ of the contact area between two grain can be assimilated to the size of the hot spots. Here, the sizes ϕ are identified as a function of the hot spot temperature T_h using Eq. 5. T_h is varied from 2 K to the Nb transition temperature $T_c \sim 9.2$ K. Four distinct curves are shown in Fig. 3. corresponding to different bulk temperatures T_0 of the inner cavity wall, namely, 2, 3, 4 and 5 K. Here, all calculations are performed at a fixed surface magnetic field of $B_z = 100$ mT for a cavity running at a frequency $f=1$ GHz. We chose these parameter values as they represent typical physical conditions under which hot spots are observed at test facilities/laboratories. As shown in Fig. 3 the hot spot sizes ϕ induced by the surface electric field lie between ~ 10 μm and ~ 100 μm . There is an increasing impact on the hot spot temperature for ϕ -values greater than ~ 20 μm . These orders of magnitude of ϕ are in very good agreement with grain sizes generally found in polycrystalline niobium used in the fabrication of SRF cavities. Another interesting feature put to evidence

in Fig. 3 is the parabolic behavior of ϕ with T_h . This behavior is due to the strong temperature dependency of London penetration depth λ_L , especially for hot spot temperatures above ~ 6 K. At T_c , λ_L diverges and therefore ϕ drops to zero.

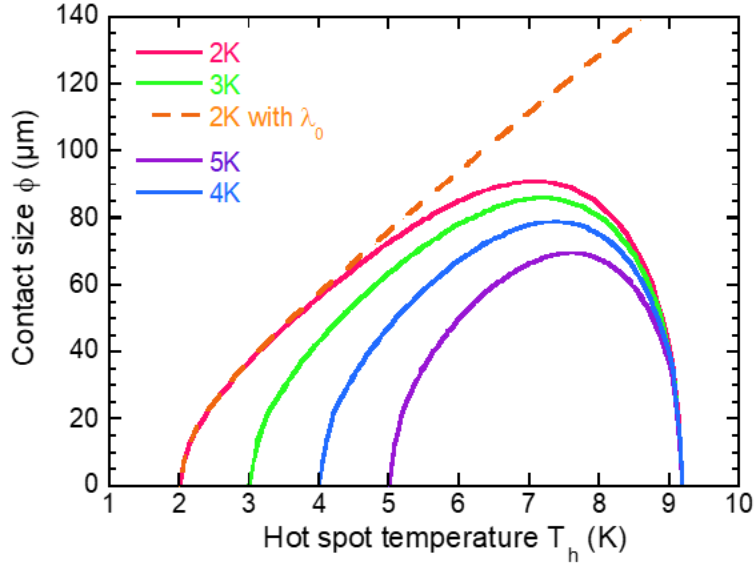


Figure 3. Identification of hot spot sizes susceptible to come into play as a function of the hot spot temperature. B_z is set to a constant typical value of 100 mT and the $f = 1$ GHz. The different curves correspond to different global temperatures T_0 of the inner surface. For $T_0 = 2$ K the dashed line represents ϕ -values when the temperature dependency of the London penetration depth is neglected in Eq. 5. The non-linear behaviour of all the solid line curves is due to the temperature dependency of the London penetration depth. (color online).

The dashed line in Fig. 3 shows ϕ -values for a constant $\lambda_L(T = 2K) = \lambda_0$. For an inner surface temperature of $T_0 = 2$ K the discrepancy between the dashed line with λ_0 and the solid red curve with $\lambda_L(T)$ clearly illustrates the impact of the temperature dependency of the London penetration depth $\lambda_L(T)$. Fig.3 also shows that smaller ϕ play an increasingly important role as the bulk temperature of the inner wall T_0 increases. Finally, we note that it follows from Fig. 3 that same hot spot diameters ϕ are present at different inner surface temperatures T_0 of the cavity. Therefore, it is also clear from Eq. 5 that the same hot spot diameters ϕ are effective at different frequencies and surface magnetic fields.

To compare our model predictions with experimental observations of SRF cavity behavior, we calculate the temperature T_h of hot spots as a function of the surface magnetic field B_z which is varied from 0 to 250 mT with the frequency f set to 1 GHz. Since λ_L depends on T_h , the calculations are performed iteratively until both T_h and $\lambda_L(T_h)$ converge. Figures 4 (a) to (d) shows the results for bulk inner wall temperatures set to 2, 3, 4 and 5 K respectively. In each of these graphs the contact size is varied from 10 μm to 100 μm .

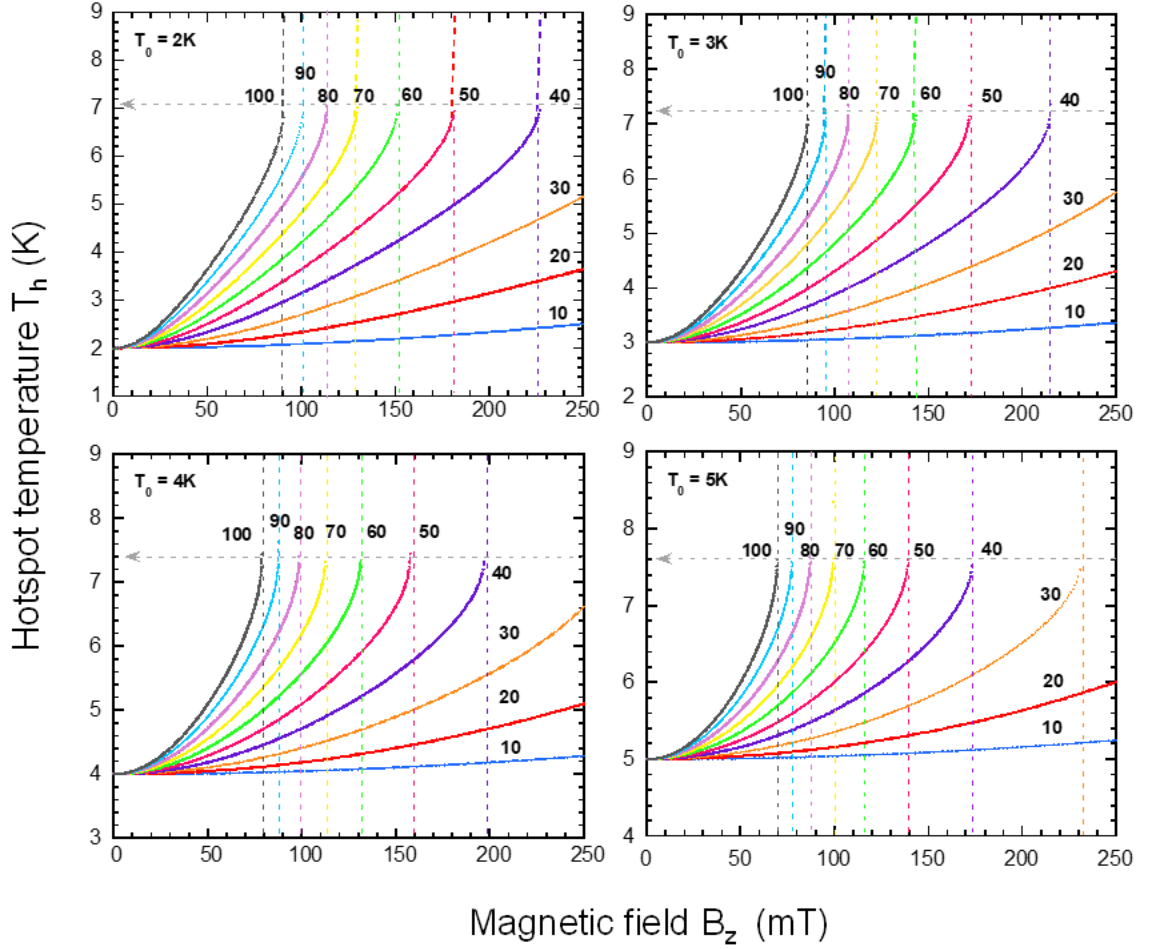


Figure 4. Hot spot temperature evolution as the surface magnetic field is increased from 0 to 250 mT for different contact sizes ranging from 10 μm to 100 μm (unites not shown). The calculations are conducted at four different inner surface temperatures, namely $T_0 = 2, 3, 4$ and 5K; and for a unique frequency set to $f = 1$ GHz. The vertical dashed lines are added to highlight the shift of B_Q to lower fields as T_0 increases for

identical ϕ . The arrow heads of the horizontal dashed line indicate the T_Q associated to each T_0 . (color online).

For $\phi \leq 20 \mu\text{m}$ the increase in T_h with B_z is noticeable, indicating the presence of power dissipation. Also, the increase in T_h does not exceed $\approx 1 \text{ K}$ at the highest B_z field. For $\phi \geq 30 \mu\text{m}$ all curves show spectacular increases in T_h by several kelvins with B_z . The rate of change of T_h with B_z steepens to become exponential-like for larger ϕ values or when the bulk inner wall temperature increases (compare curves between Figs. 4 (a) and 4 (d)). All these graphs demonstrate the importance of surface electric fields in inducing a coherer-like effect which results in dissipating heat at grain boundaries/cracks.

As shown in Fig. 4 (a)-(d), our model captures another major feature which is the onset of the Q-drop. This is characterized by a sharp increase of the hot spot temperature from a critical value T_Q , which we call the onset temperature of Q-drop. Associated to T_Q , we define the magnetic field B_Q for the onset of Q-drop. All curves plotted in Fig. 4 (a) to (d) were obtained by iteration for temperatures $T_h \leq T_Q$ where the SRF cavity is stable. As shown in Fig. 4 (a)-(d), at B_Q the temperature at the hot spot T_Q is not the transition temperature of niobium. The temperatures T_Q reach values which are $\approx 7 \text{ K}$, but differ slightly from curve to curve depending on the value of T_0 . Now, by expanding equation 5 in a polynomial form, a generalized expression is derived for the onset temperature T_Q of Q-drop (as described in the Appendix):

$$T_Q = \frac{1}{\sqrt{3}} \left[T_0^2 + \sqrt{T_0^4 + 3T_c^4} \right]^{1/2} \quad (7)$$

Interestingly, T_Q depends only on T_0 and T_c . Since T_c is a constant, T_Q is entirely determined by T_0 . As can be seen from the dashed horizontal lines in Fig. 4 (a) to (d), the values predicted by equation (7) are in excellent agreement with those found by iteration for different T_0 .

The Q-drop is generally observed for typical values of B_z lying in the range 90 -150 mT. From Fig. 4 (a)-(d) we can therefore identify that contact sizes ϕ in the range $\sim 40 \mu\text{m}$ to $100 \mu\text{m}$ play a predominant role, depending upon the bulk inner wall initial temperature T_0 . It is important to note that the frequency is set to a constant value of 1 GHz in Fig. 4 (a)-(d). As is evident from equation 5, identical temperature shifts are possible for different contact sizes ϕ depending upon the frequency and will be discussed later.

To get an understanding of the behavior of the critical magnetic fields B_Q at which Q-drop is activated, we plot in Fig. 5 the B_Q -values (dots) calculated by iteration in Fig. 4 (a)-(d), as a function of the inner wall temperature T_0 for different ϕ and with $f = 1$ GHz. Here, the solid curves going through the dots are obtained from substituting Eq. (7) in Eq. (5) (details in Appendix). There is an excellent consistency between the results obtained by iteration (dots) and the curves. Fig. 5 shows that the highest B_Q values are reached for contact sizes $\phi \leq 20 \mu\text{m}$. For $\phi \geq 50 \mu\text{m}$ there is the significant decrease in B_Q with the contact size ϕ , in accordance to the behavior $B_Q \propto \frac{1}{f\phi}$ from Eq. (5) (also see equation A4 in Appendix) when T_0 and T_Q are constants. Fig. 5 also shows that B_Q shifts to lower fields with increases in T_0 for a constant ϕ .

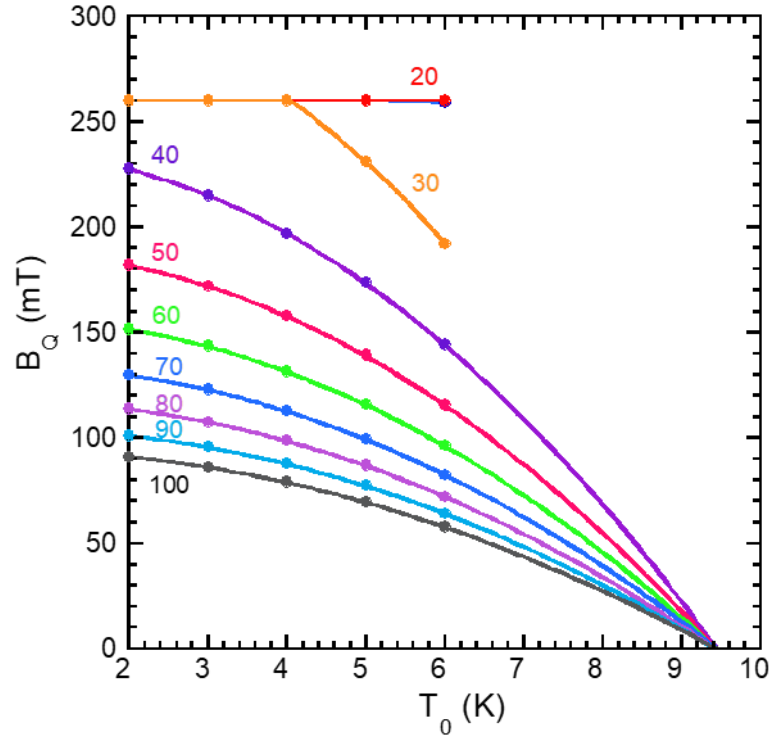


Figure 5. Magnetic field B_Q (in mT) for onset of Q-drop as a function of the inner wall temperature T_0 . Each curve corresponds to a given contact size. Here $f = 1$ GHz for all curves. The dots are obtained by iteration from Eq. 5. The solid curves are calculated curves (see Eq. A4). For $\phi \leq \sim 20 \mu\text{m}$, B_Q remains at constant. For $\phi \sim 30 \mu\text{m}$, B_Q begins to decrease when $T_0 \geq 4$ K. For $\phi \geq 35$, B_Q decreases with T_0 and ϕ . (color online)

Now, T_0 is affected by the Joule dissipation due to the interaction of the magnetic field B_z with the rf surface resistance R_s . The increase in T_h due to the coherer effect modifies the rf surface resistance $R_s(T_h)$ at the hot spot and consequently alters the local Joule dissipation P_j due to the magnetic field interaction with the surface resistance. Our model thus reveals a surface magnetic field-dependence of R_s . The importance of maintaining a low T_0 working temperatures is also clearly a necessity as apparent in our model.

The vertical dashed curves in Fig. 4 (a)-(d) captures the behavior of $T_h(B_z)$ beyond T_Q where the SRF cavity becomes prone to be thermally unstable, depending on the sizes and the numbers of hot spots. These curves are obtained at $T_h > T_Q$ by numerical iteration under non-equilibrium conditions. The non-equilibrium conditions mean that the strict convergence criterion during the iterations to determine the T_h which satisfies Eq. 5, is loosened by allowing an uncertainty on the T_h -value because of the strong nonlinear behavior of $\lambda_L(T)$. Under these conditions, we put to evident the hallmark of Q-drop. Indeed, as seen from Fig. 4 (a)-(d), during Q-drop T_Q increases to $\sim T_c$ for all contact sizes greater than $\sim 50 \mu\text{m}$. We note that as B_Q is approached, the B_z fields are incremented in steps not exceeding 0.5 mT (0.2 mT for all $\phi \geq 60 \mu\text{m}$). Above B_Q very small increases in B_z induce steep increases in the hot spot temperature to above T_Q , and eventually to T_c . These findings indicate that hot spot temperatures in the neighborhood of T_Q are extremely sensitive to B_z and, consequently to infinitesimal modifications in the electric field E_y . This provides a clue as to why slight changes in the impurity content due to baking or any purification treatment of Nb [15] which may provoke changes in E_y and therefore result in shifts in the B_Q -field values after treatment.

For cases where a Q-drop has been reported with small size grains, we evoke the possibility of an effect arising from a cluster of grain contacts. A cluster of small grains joints (of the order of $\sim 10 \mu\text{m}$ or much less, depending upon the global temperature of the inner wall) can collectively dissipate sufficient power equivalent to a single large grain joint.

Fig. 6 shows the evolution of the hot spot temperature as a function of the local electrical field strengths E_y which comes into play. The magnitudes of E_y (expressed in V/m) are determined using the equation $E_y = 2\pi f \lambda_L(T) B_z$, with B_z -values which satisfy Eq. 5 when $T_h \leq T_Q$. The overall bulk temperature is kept at $T_0 = 2 \text{ K}$ with the frequency $f = 1 \text{ GHz}$, for contact sizes ranging from $20 \mu\text{m}$ to $100 \mu\text{m}$. The strong

dependency of T_h on the electric field and on the contact size ϕ are clearly demonstrated. For contacts of $\phi \sim 20 \mu\text{m}$, electric fields of the order of $\sim 35 \text{ V/m}$ suffice to create over-heating of $\sim 1 \text{ K}$.

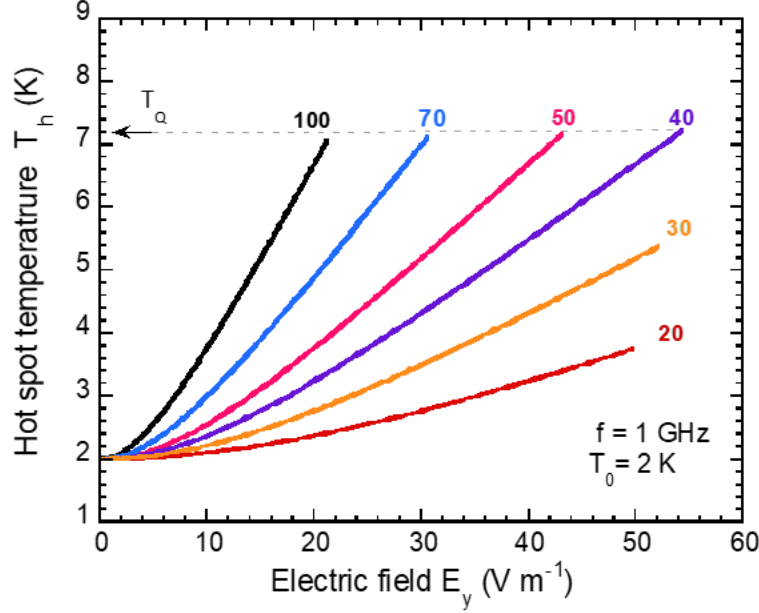


Figure 6. Evolution of the hot spot temperature from $T_h = 2 \text{ K}$ as a function of the electric field strength E_y present in the material (see Eq. 4). Six hot spot sizes ranging from $20 \mu\text{m}$ to $100 \mu\text{m}$ are shown in the figure. (Units are omitted in figure for clarity). At a given electric field, the influence of the size of the contact on the hot spot temperature is clearly evident in the figure. (color online)

As ϕ increases, much smaller electric fields generate hot spots whose temperatures reach T_Q . Each curve for a given ϕ in Fig. 6 is implicitly dependent on f . Increasing the frequency leads to an increase in the E_y -field and consequently to an increase in T_h according to Eq. 4. Finally, we note that the surface electric fields E_y are approximately a factor of 10^5 times smaller than the accelerating gradient E_a .

3.3. Power dissipation and current densities at hot spots

Following Holm [22], the electrical contact (or “constriction”) resistance between two grains of the same material is given as $R(\phi) = \rho_0 \frac{\ell}{A} = \frac{\rho_0}{\pi\phi}$, where ρ_0 in our case is the residual surface resistivity of niobium

below T_c and is taken to be $\rho_0 = 5 \text{ n}\Omega \text{ m}$, the length $\ell \approx \phi$ and A is the contact surface area. The lines of current are constraint to flow across the contact between two grains and they induce local ohmic heating. The electrical power dissipated is given by $P_E = \varphi^2/R = \frac{\pi\phi^3 E_y^2}{\rho_0}$. Since $E_y = -j\omega\lambda_L B_z$, the dissipated power can be expressed as:

$$P_E = \frac{\pi\phi^3(2\pi f)^2\lambda_0^2 B_z^2}{\rho_0 \left[1 - \left(\frac{T_h}{T_c}\right)^4\right]} \quad (8)$$

Eq. (8) clearly reveals all parameters which impact power dissipation during heating by the coherer effect. The P_E strongly depends on the contact size ϕ , the frequency f , the surface magnetic field B_z and the hot spot temperature T_h . Further, the temperature dependency of P_E due to the London penetration depth leads to a “snowball” effect as T_h becomes greater than T_Q during Q-drop.

Fig. 7 (a) shows estimates of the dissipated power $P_E(B_z)$ for contact sizes of 30, 40, 50, 70 and 100 μm . As before, the iterations are conducted for $f = 1 \text{ GHz}$ and $T_0 = 2 \text{ K}$ with B_z -values that satisfy equation 5.

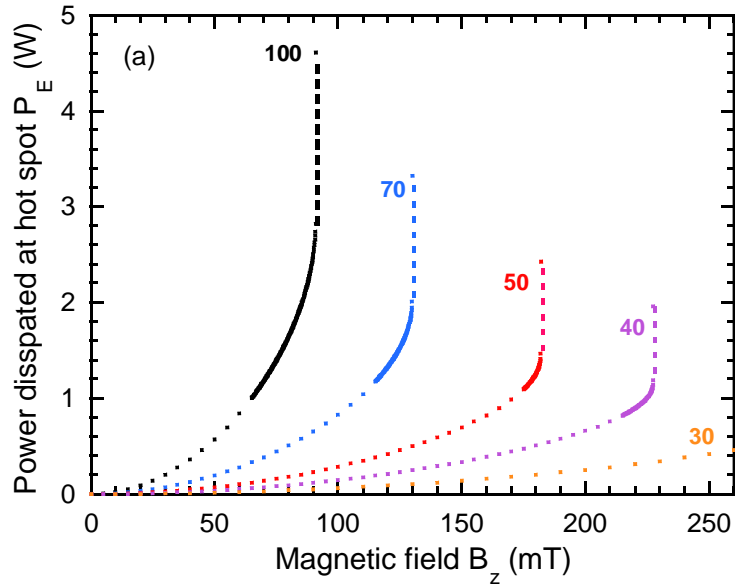


Figure 7 (a). Our model predictions of power dissipated as a function of the surface magnetic field B_z at contacts of different sizes. All calculations are done for a fixed $f = 1 \text{ GHz}$ and $T_0 = 2 \text{ K}$. As B_z approaches

B_Q the power dissipation becomes exponential-like. The solid lines are due to an increased refinement in the B_z -field increments. There is a sharp instantaneous increase in P_E as B_z surpasses B_Q . At the maximum powers for each ϕ , the hot spot temperature lies within the range $7 \text{ K} < T_h < 9.2 \text{ K}$. Note the increase of the maximum power with ϕ . (color online)

For $B_z \leq B_Q$ the dissipated power increases at different rates, depending on the size of the hot spot. As B_z is increased beyond B_Q the power increases almost instantaneously for all contact sizes greater than $35 \mu\text{m}$. As can be seen in Fig. 7 (a), the maximum power dissipated varies from a few milliwatts for $\phi = 10 \mu\text{m}$ (not shown in Fig. 7) to a few watts for $\phi = 100 \mu\text{m}$. At the maximum powers shown in this figure, T_h lies between T_Q and $\sim 9.2 \text{ K}$ (Nb transition temperature) for all $\phi \geq 40 \mu\text{m}$. The global temperature of the inner wall does not significantly alter the magnitude of the powers that are dissipated at identical contact sizes.

Fig. 7 (b) shows the power dissipated $P_E(T_z)$ for different contact sizes. For all contact sizes greater than $\phi \geq 35 \mu\text{m}$, the hot spot temperature evolves from its initial temperature $T_h = 2 \text{ K}$ to T_Q as the magnetic field B_z is increased to B_Q . It is interesting to note that Fig. 7 (b) reveals that for $\phi < 35 \mu\text{m}$, hot spots do

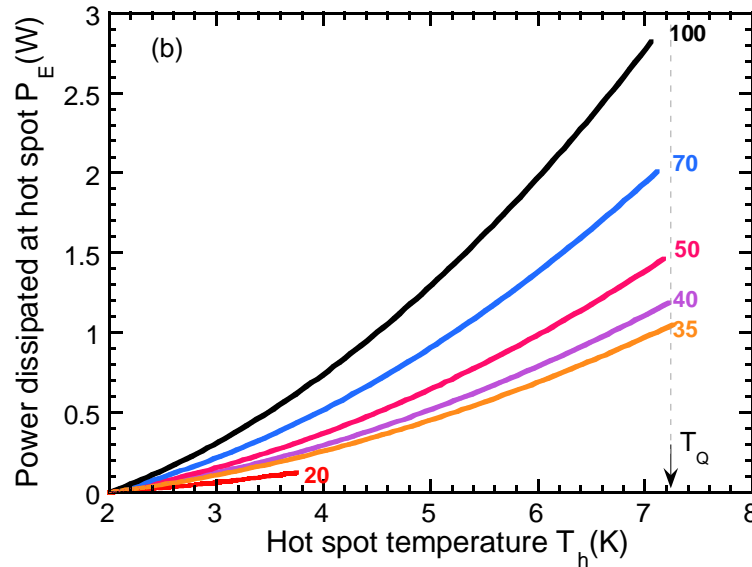


Figure 7 (b). Power dissipation due to the electric field at hot spots of different sizes (in μm) as a function of the hot spot temperatures not exceeding T_Q , where B_Q is reached for all $\phi \geq 35 \mu\text{m}$. Here $T_0 = 2 \text{ K}$ and $f = 1 \text{ GHz}$. Under these conditions, note that $P_E < \sim 0.1 \text{ W}$ for all $\phi < 20 \mu\text{m}$.

do not reach T_Q at the maximum B_z field which here is set to 250 mT.

The current density across the contacts is defined in the usual way as $j_E = \varphi/(AR) = E_y/\rho_0$. The E_y -values are determined iteratively from Eq. 5 as explained above. The j_E dependency on frequency, hot spot temperature and the surface magnetic field is implicit in the equation. Indeed, the electrical contact resistance R plays a determinant role as well. Fig. 8 (a) shows the electric current density j_E as function of B_z for different contact sizes for $f = 1$ GHz and $T_0 = 2$ K. Fig. 8 (a) shows that j_E increases linearly with B_z at almost the same rate for all contact sizes. As the B_Q -fields are approached, the j_E -values deviate from their linear behavior and undergo a sharp increase for all contact sizes $\phi \geq 35 \mu\text{m}$. Fig. 8 (b) shows that the $j_E(T_h)$ present across the contacts do not exceed $\sim 4 \times 10^7 \text{ A cm}^{-2}$ for all ϕ -values as long as $T_h < T_Q$. And, the maximum current densities decrease with contact sizes for all $\phi \geq 50 \mu\text{m}$.

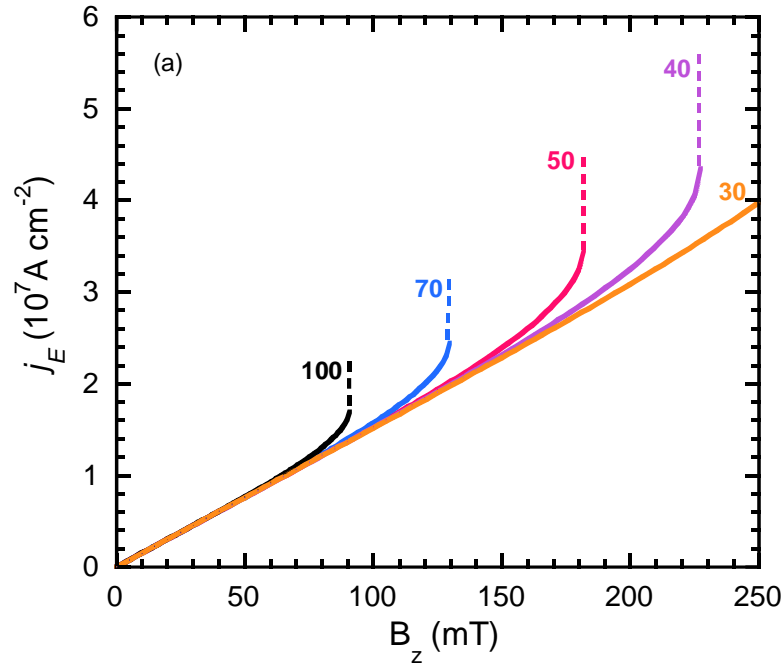


Figure 8 (a). Estimates of the current density at hot spots of different sizes (indicated in μm in the figure) as a function of the surface magnetic field. The current densities jump sharply as B_Q is reached for contacts sizes $\phi \geq 35 \mu\text{m}$. The resolution of curves (full curve to dashes) is an artifact of the numerical increment in B_z -values above B_Q . (color online)

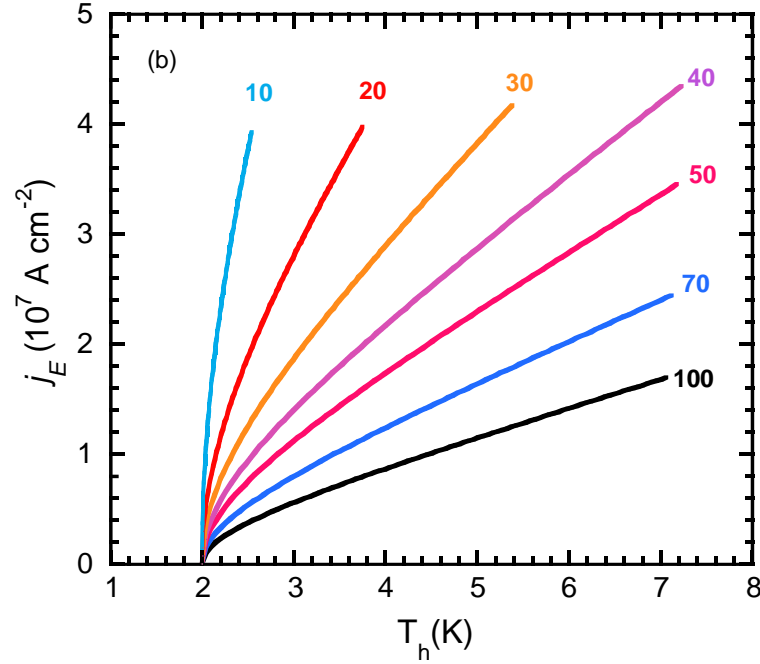


Figure 8 (b). Current densities j_E as a function of hot spots temperatures $T_h \leq T_Q$ for contact sizes ranging from 10 to 100 μm (units not shown). Calculations are done for $f = 1$ GHz. For all $\phi < 40$ μm , j_E reach maximum values of $\sim 4 \times 10^7$ A cm^{-2} . For $\phi > 40$ μm , j_E decreases with ϕ and reaches maximum stable values at $T_h = T_Q$. (color online)

4. Thermal diffusion from hot spots to helium bath

Heat dissipated at the hot spot sites on the inner wall propagate to the outer wall where it is evacuated into the surrounding superfluid He II. Since the Nb thickness is ~ 3 mm and depending on the purity on the Nb, the phonon mean free paths are limited by the walls and therefore “patches” of hot spots occur on the outer cavity surface. In Ref. [23] Ciovati *et al.* conducted thermal mapping of these hot spots on a single-cell SRF elliptical cavity wall immersed in superfluid helium. Using carbon resistors placed in a network configuration on the outer surface, the location and the local temperature increase δT of hot spots were measured. The δT values lie between 0.1 and 0.7 K, and the hot spot sizes are identified to spread over lengths of ~ 1 cm. The evacuation of heat into the surrounding superfluid is limited only by the thermal boundary Kapitza resistance R_K , which is extensively studied in ref. [24,25]. The powers evacuated from a hot spot “patch” on the outer surface to the surrounding He II is given by $\dot{Q} = S\delta T/R_K$. For a bath temperature

maintained at 1.8 K and taking $R_K \approx 2 \text{ cm}^2\text{K/W}$ [25], we estimate that \dot{Q} falls within the range 0.01-0.5 W over a typical value of a surface $S = \pi \times 0.5^2 \text{ cm}^2$. These \dot{Q} values are in very good agreement with our model predications of the powers dissipated at hot spots on the inner surface as can be seen from Fig. 8 (a). Indeed, under steady state conditions the heat flux flowing out into the superfluid coolant is equal to the heat dissipated at the hot spot. But the heat flow path is nonlinear and the lateral distance on the plane of the outer surface over which the heat is evacuated to the superfluid is much larger than the Nb thickness. In summary, the present estimations support our model, but a detailed analysis heat of heat evacuation to superfluid He, including heat sources P_J and P_E is necessary.

5. Discussions

Although we adapt the formulation of the coherer mechanism to cast a model that explains the origin of hot spots in SRF cavities, the coherer effect which eventually results in the fusion of grains does not occur in our model. However, the salient feature in common with our model is the constriction of the surface current flow at portions of grain boundaries as in the coherer effect (see Fig. 1(b)). Our proposed mechanism identifies the different key parameters which come into play and therefore shows a new pathway to minimize and to overcome the formation of hot spots.

5.1 Contact diameter at hot spots

For simplicity we define in our model the diameter of the contact hot spot site between grains by a single parameter ϕ . The contact geometry can certainly be characterized with more refinement based on material science studies of polycrystalline niobium, but it will not change the fundamental outcome of the conclusions in this study. Micro-cracks on the surface also constitute sites for formation of hot spots. In the case of contact between rough surfaces, multiple discrete contact points, each of diameter ϕ_i , between the two surfaces lead to a global constriction resistance over an effective diameter ϕ_{eff} . In such a case our ϕ corresponds to ϕ_{eff} . We also note that the grain sizes are evidently always greater than ϕ and consequently the granularity of polycrystalline material for which our calculations are performed has to be much greater than the ϕ -values we have determined. In a more realistic description, it is also clear that there must be a distribution of contact

sizes which come into play within the material. Taking into account this distribution in a model should lead to refinement in capturing the thermal behavior depicted in experimental observations (see for example Figs. 5.7 & 5.15 in ref. [14]). These figures show clusters of hot spots of different intensities. Although our model is derived for a single hot spot, the feature is inferred by Eq. 5.

5.2 Comparison with experimental findings

The onset of Q-drop is governed by power dissipation in the inner cavity walls. In this study we have shown that our model predicts a steep increase in the electrical power dissipated at a hot spot of a given diameter as B_Q is approached (see Fig. 7). These steep increases in power induces the onset of the Q-drop effect. The B_Q -values shown in Fig. 7 are remarkably consistent with those values of the magnetic field where Q-drop is observed (see for example [26, 27, 28]). As evident from experimental plots of the Q-factor as a function of the magnetic field, (see Figures 6 & 9 in ref. (23)) their slopes ($\partial Q/\partial B_z$) vary from curve to curve according to the treatment of the niobium. In light of our model, we believe that this feature depends on the number of hot spots, their diameter size distribution, the frequency of the magnetic field, the intensity of the surface electric field and most importantly it depends on modifications in the electrical contact resistance R , at grain boundaries or cracks due to the various treatments like baking. As pointed-out in ref. [29], the process of baking would allow a redistribution of oxygen. Also underlined in ref. [30] is the fact that progressive baking at higher temperatures leads to a transformation of the external Nb_2O_5 layer into metallic sub oxides (NbO , NbO_2) into the niobium. The study of the grain boundary structure with high resolution TEM shows the presence of surface defects due to impurity segregations, oxide phases and dislocations pile-ups in the vicinity of grain boundaries [31]. Owing to these processes, R undergoes changes (even at nanometer scales) which must modify power dissipation. Consequently, $(\partial Q/\partial B_z)$ and B_Q for Q-drop must be altered. The conjecture pertaining to modifications in R also tend to support the experimental findings namely, (i) the electro polished Nb surface generally reach higher field than cavities which are chemically etched with BCP (see chap. 5 and ref. [14,26]) and (ii) hot spots at the irises of the cavity, which are high electric fields areas, occur after baking in air at 180°C. In the latter case, the temperature increase of the hot spots exceeded 1 K for tests being performed at 1.7 K (see Fig. 7(b) and 7(d) in Ref. [23]). Finally,

we add that, by measuring current transport at grain boundaries, significant variations in grain boundary properties due to surface chemical treatment (BCP or electro polishing) are shown in Ref. [32].

Hot spots are observed [23] in the TM_{010} mode, where electric and magnetic fields are present on the surface, and also in the TE_{011} modes, where the electric field is theoretically absent [29] on the surface. We believe that power dissipation due to the surface magnetic and electric fields, given respectively in this paper by expressions of P_J and P_E , are independent mechanisms, but they impact one another when they operate simultaneously. This may explain the difference in the two experimental data of the Q-factor versus the magnetic field in the TM_{010} and TE_{011} modes shown in Fig.9 of Ref. [29]. Following our conjecture, there is evidently more dissipation in the TM_{010} mode than in the TE_{011} mode where the coherer effect maybe absent or strongly attenuated, depending on the repartition of the surface electric and magnetic fields which play a decisive role (see Fig. 1 in ref. [29]) here. These arguments are quantitatively consistent with the fact that the Q-factor and the onset magnetic field for Q-drop are lower in the TM_{010} mode as observed in Fig.9 of Ref. [29].

5.3 Dislocations

Dislocations play a strong role in the thermal conductivity of a material. The thermal conductivity across grains is also hampered by the presence of dislocations in their vicinity. It is well-known that dislocations play an important role in flux pinning of vortex lines in type II superconductors [33] which leads to an increase in the critical current. Another possible consequence of the presence of dislocations is the shift in the superconducting transition temperatures [34]. All these effects are temperature dependent and must therefore influence R and hereby impact the electric power dissipation to extents that need to be quantified in future models.

5.4 Similarities with Josephson type nano-junctions

Tinkham *et al.* [35] demonstrated that a Nb/oxide/Nb configuration behaves as a Josephson junction when the oxide layer is only a few nanometers thick. Using a 1D model, they analyzed heating effects in high

frequency Josephson devices. They showed that the temperature at the center of the junction as the following behavior as a function of the applied voltage φ :

$$T_h = \left(T_0^2 + 3 \left(\frac{e\varphi}{2\pi k_B} \right)^2 \right)^{1/2} \quad (9)$$

where e is the electric charge and k_B is the Boltzmann constant. Noting that $L = \frac{\pi^2 k_B^2}{3e^2}$, Eq. (9) turns out to be identical to our Eq. (3). In their calculations, the constriction forming the junction is taken to have a hyperbolic neck geometry.

Using a quantum mechanical picture, Halbritter [10,9] also considered the oxide-filled boundaries on Nb for SRF cavities to act like Josephson junctions. The interface tunneling exchange (ITE) process is made possible due to the presence of a high density of localized states ($\sim 10^{19} \text{ cm}^{-3}$) in the oxide layer. This tunneling phenomenon is due to an “overflow” of the cooper pair wave function from the superconducting material into the oxide layer (which is in a normal state). The current densities of the order of $j_E \approx 10^7 \text{ A/cm}^2$ were estimated for these junctions [9]. These values are in excellent agreement with estimates of j_E using our model shown in Fig. 8(b).

In the case of Nb films, Junginger *et al.* [11] showed that, instead of the magnetic field, the electric field dominates losses for strongly oxidized Nb films due to the ITE mechanism at grain boundaries. In these pictures the presence of a nanometer thick oxide layer is mandatory at grain joints. This is not necessarily the case at grain joints at the surface in bulk Nb samples that we have considered. But, we cannot exclude the ITE process since it is possible for the oxide layer to be sufficiently thin such that contacts may form Josephson-like junctions on the Nb surface, as discussed by Tinkham *et al.*[35]. In this case, our model estimates the temperature rise and heat dissipation from a nanometer-size contact location to be very small compared to hot spots with $\phi \geq 20 \text{ }\mu\text{m}$ as described in the present work. However, a conglomeration of nanometer-size contacts will undoubtedly lead to observable temperature increases. We also note that the models discussed in this section, including our model, require the presence of an electric field, however small.

6. Conclusions

In this study, we build a model based on a novel electro-thermal mechanism which explains the occurrence of hot spots at portions of grain boundaries and/or at micro cracks in SRF niobium cavities. In

our model, heating is due to the presence of a surface electric field which induces electron current lines, analogous to a coherer-type effect, but at liquid helium temperatures in our case. The constriction of these current lines across portions of grain boundaries/cracks produces local power dissipation which form hot spots. The temperature of the hot spot is derived as a function of its size, the local surface electric fields generated by the surface magnetic fields of different frequencies and the London penetration depth (Eq. 5). The typical sizes of the hot spots are identified to lie generally within the range of 10-100 μm . Our model also provides a phenomenological description of Q-drop observed above a critical surface magnetic field (and therefore electric field). The critical magnetic fields B_Q reached at the onset of Q-drop is strongly controlled by the temperature dependency of the London penetration depth, the frequency and the hot spot size. The powers and current densities at hot spots of various sizes are calculated as a function of B_z and T_h . There is, ultimately, a very good quantitative agreement between observations of hot spots on SRF niobium cavities reported in the literature cited in this paper and our model predictions. Our theory sets a basis for a new pathway to understand hot spots by taking into account the surface electric fields.

Acknowledgements

We are grateful to Claire Z. Antoine of CEA/Saclay who introduced us to the subject of hot spots in SRF cavities a few years ago. This work benefited from discussions with members of the Irene Joliot-Curie Laboratory (IJC Lab in Orsay), especially Guillaume Martinet and Mohammed Fouaidy. We are indebted to Aurore Amrit for helping with the computational work. One of us (AR) acknowledges support by the Shenzhen University start-up fund (No. 860-000002110199)

Appendix: Temperatures and magnetic fields at onset of Q-drop

Here we present a derivation of the critical temperature T_Q and magnetic field B_Q at which the onset of Q-drop is triggered. Eq. 5 is the main equation describing the temperature evolution at hot spots during dissipation due to the coherer-like effect induced by the surface electric fields in our model. Various parameters play a role in this equation including the magnetic field, the frequency, the hot spot size, the London penetration depth and the global temperature of the inner surface of the SRF cavity:

$$T_h^2 = T_0^2 + \frac{(2\pi f)^2 \lambda_0^2 B_z^2 \phi^2}{4L(1 - (T_h/T_c)^4)} \quad (\text{A1})$$

This non-linear equation does not have an exact analytic solution and it is therefore solved iteratively.

Now, expanding (A1) we can rewrite it in a polynomial form $P(T_h) = 0$:

$$\frac{T_h^6}{T_c^4} - T_0^2 \frac{T_h^4}{T_c^4} - T_h^2 + T_0^2 + \frac{(\pi f)^2 \lambda_0^2 B_z^2 \phi^2}{L} = 0 \quad (\text{A2})$$

Taking f , ϕ and B_z in the last two terms to be independent on T_h , then solving for the roots of $(dP/dT_h) = 0$ yields the critical values of T_Q for which (A2) is a maximum. The calculation is straightforward and it has only one positive solution:

$$T_Q = \left(\frac{T_0^2 + \sqrt{T_0^4 + 3T_c^4}}{3} \right)^{1/2} \quad (\text{A3})$$

Rather surprisingly T_Q depends only on T_0 and T_c . Substituting (A3) in (A1) defines the critical magnetic field at T_Q :

$$B_Q = \frac{\sqrt{L}}{\pi \lambda_0} \frac{g(T_0, T_Q, T_c)}{\phi f} \quad (\text{A4})$$

where $g(T_0, T_Q, T_c) = \left[(T_Q^2 - T_0^2) \left(1 - (T_Q/T_c)^4 \right) \right]^{1/2}$. Although T_Q is entirely determined by the inner surface temperature of the SRF cavity, the magnitude of B_Q varies with all the key parameters in the model, namely T_0 , T_Q , ϕ and f .

Using Eq. (4) we introduce the critical electric field E_Q associated with B_Q ; and consequently,

$g(T_0, T_Q, T_c) = (E_Q \phi / 2\sqrt{L}) (1 - (T_Q/T_c)^4)^{1/2}$. Eq. (A4) now simplifies to the well-known expression:

$$B_Q = \frac{E_Q}{2\pi f \lambda_L(T_Q)}$$

References

- [1] A. Gurevich, Phys. C Supercond. **441**, 38 (2006).
- [2] T. Kubo and A. Gurevich, Phys. Rev. B **100**, 064522 (2019).
- [3] G. Ciovati and A. Gurevich, Phys. Rev. Spec. Top. - Accel. Beams **11**, 122001 (2008).
- [4] A. Gurevich, Supercond. Sci. Technol. **30**, 034004 (2017).
- [5] P. Bauer, N. Solyak, G.L. Ciovati, G. Ereemeev, A. Gurevich, L. Lilje, and B. Visentin, Phys. C Supercond. **441**, 51 (2006).
- [6] V. Shemelin and H. Padamsee, TTC-Report 2006-07 **SRF 080903**, (2008).
- [7] J. Knobloch, R.L. Geng, M. Liepe, and H. Padamsee, 9th Work. RF Supercond. (SRF 1999) 77 (1999).
- [8] A. Gurevich and G. Ciovati, Phys. Rev. B - Condens. Matter Mater. Phys. **87**, (2013).
- [9] J. Halbritter, in *10th Work. RF Supercond.* (Tsukauba, Japan, 2001), pp. 292–301.
- [10] J. Halbritter, J. Appl. Phys. **97**, 083904 (2005).
- [11] T. Junginger, S. Aull, W. Weingarten, and C.P. Welsch, IEEE Trans. Appl. Supercond. **27**, 1 (2017).
- [12] T. Junginger, M. Heidelberg, R. Seviour, and W. Weingarten, in *IPAC2011* (San Sebastian, Spain, 2011), pp. 310–312.
- [13] A. Romanenko and D.I. Schuster, Phys. Rev. Lett. **119**, 264801 (2017).
- [14] H. Padamsee, *R. F. Superconductivity: Science, Technology and Applications* (Verlag GmbH & Co., 2009).
- [15] G. Ciovati, G. Myneni, F. Stevie, P. Maheshwari, and D. Griffis, Phys. Rev. Spec. Top. - Accel. Beams **13**, 022002 (2010).
- [16] C.Z. Antoine, Phys. Rev. Accel. Beams **22**, 34801 (2019).
- [17] M. Creyssels, S. Dorbolo, A. Merlen, C. Laroche, B. Castaing, and E. Falcon, Eur. Phys. J. E **23**, 255

(2007).

- [18] E. Falcon, B. Castaing, and M. Creyssels, Eur. Phys. J. B **38**, 475 (2004).
- [19] S. Dorbolo, M. Ausloos, and N. Vandewalle, Phys. Rev. E **67**, **040302**, 040302 (2003).
- [20] F. Koechlin and B. Bonin, Supercond. Sci. Technol. **9**, 453 (1996).
- [21] H. Safa, D. Moffat, B. Bonin, and F. Koechlin, J. Alloys Compd. **232**, 281 (1996).
- [22] R. Holm, *Electric Contacts* (Springer Berlin Heidelberg, Berlin, Heidelberg, 1967).
- [23] G. Ciovati, P. Kneisel, and A. Gurevich, Phys. Rev. Spec. Top. - Accel. Beams **10**, 062002 (2007).
- [24] J. Amrit and C.Z. Antoine, Phys. Rev. Spec. Top. - Accel. Beams **13**, 023201 (2010).
- [25] J. Amrit and M.X. François, J. Low Temp. Phys. **119**, 27 (2000).
- [26] P. Bauer, G. Ciovati, H. Edwards, J. Halbritter, H. Padamsee, K. Saito, and B. Visentin, Fermilab Tech. Note TD-05-56 (2006).
- [27] G. Ciovati and P. Kneisel, 23rd Int. Linear Accel. Conf. LINAC 2006 - Proc. 324 (2006).
- [28] P. Dhakal, S. Chetri, S. Balachandran, P.J. Lee, and G. Ciovati, Phys. Rev. Accel. Beams **21**, 32001 (2018).
- [29] G. Ciovati and P. Kneisel, Phys. Rev. Spec. Top. - Accel. Beams **9**, 1 (2006).
- [30] G. Ciovati, J. Appl. Phys. **96**, 1591 (2004).
- [31] Z.-H. Sung, P.J. Lee, and D.C. Larbalestier, IEEE Trans. Appl. Supercond. **24**, 68 (2014).
- [32] Z.-H. Sung, P.J. Lee, A. Gurevich, and D.C. Larbalestier, Supercond. Sci. Technol. **31**, 045001 (2018).
- [33] P. Dhakal, G. Ciovati, and A. Gurevich, Phys. Rev. Accel. Beams **23**, 23102 (2019).
- [34] M. Li, Q. Song, T.H. Liu, L. Meroueh, G.D. Mahan, M.S. Dresselhaus, and G. Chen, Nano Lett. **17**, 4604 (2017).
- [35] M. Tinkham, M. Octavio, and W. Skocpol, J. Appl. Phys. **48**, 1311 (1977).